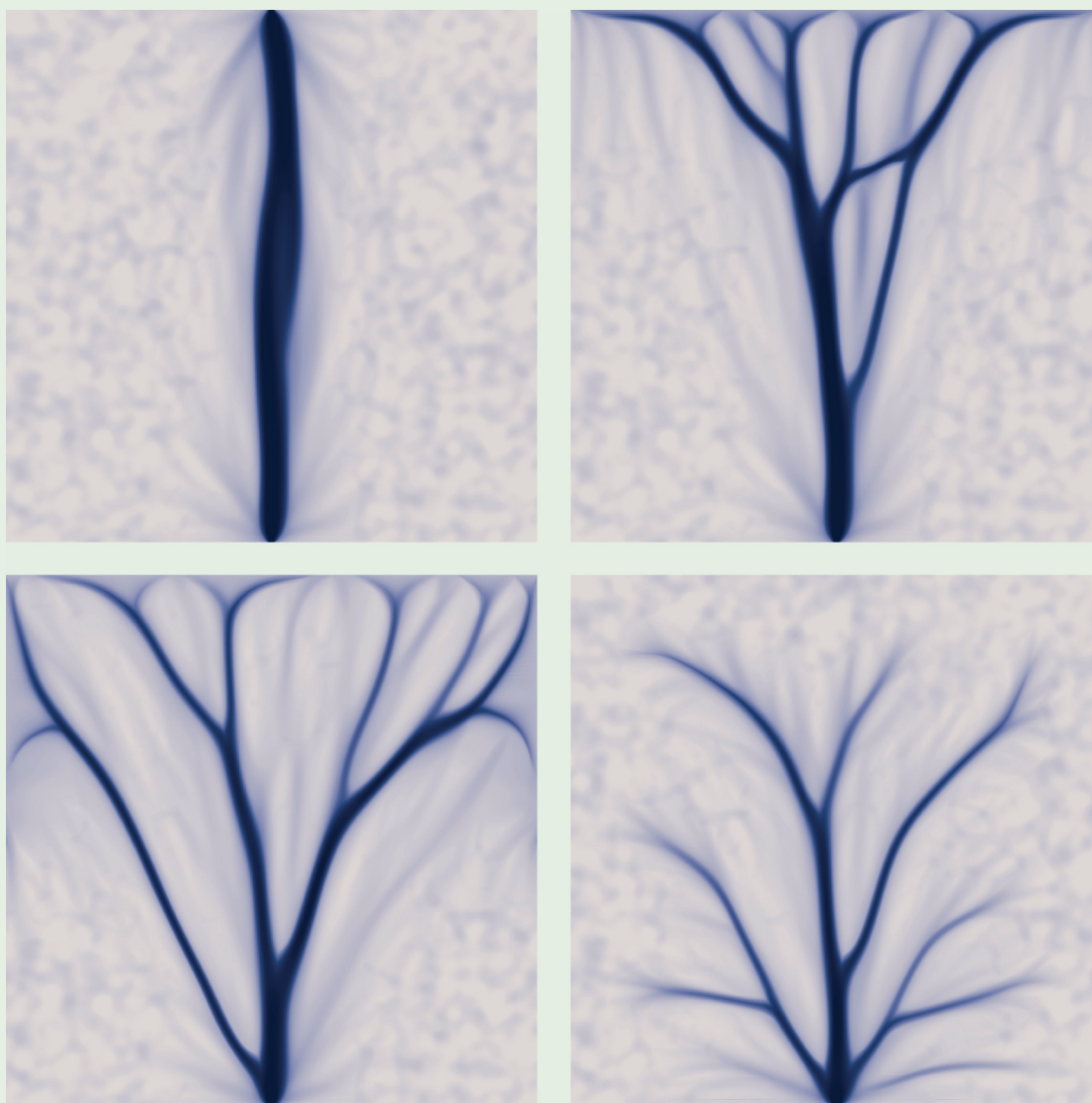


125

PHYSICAL REVIEW LETTERS

Articles published week ending

9 OCTOBER 2020



PRL 125 (15), 150401–159903, 9 October 2020 (322 total pages)

15

Published by
American Physical Society



Volume 125, Number 15

Flow-Driven Branching in a Frangible Porous Medium

Nicholas J. Derr¹, David C. Fronk², Christoph A. Weber³, Amala Mahadevan⁴,
Chris H. Rycroft^{1,5} and L. Mahadevan^{1,2,6,*}

¹John A. Paulson School of Engineering and Applied Sciences, Harvard University, Cambridge, Massachusetts 02138, USA

²Department of Organismic and Evolutionary Biology, Harvard University, Cambridge, Massachusetts 02138, USA

³Max Planck Institute for the Physics of Complex Systems, Dresden 01187, Germany

⁴Woods Hole Oceanographic Institution, Woods Hole, Massachusetts 02450, USA

⁵Computational Research Division, Lawrence Berkeley National Laboratory, Berkeley, California 94720, USA

⁶Department of Physics, Harvard University, Cambridge, Massachusetts 02138, USA



(Received 21 June 2020; accepted 18 August 2020; published 6 October 2020)

Channel formation and branching is widely seen in physical systems where movement of fluid through a porous structure causes the spatiotemporal evolution of the medium. We provide a simple theoretical framework that embodies this feedback mechanism in a multiphase model for flow through a frangible porous medium with a dynamic permeability. Numerical simulations of the model show the emergence of branched networks whose topology is determined by the geometry of external flow forcing. This allows us to delineate the conditions under which splitting and/or coalescing branched network formation is favored, with potential implications for both understanding and controlling branching in soft frangible media.

DOI: [10.1103/PhysRevLett.125.158002](https://doi.org/10.1103/PhysRevLett.125.158002)

Branching patterns in porous media are common in many natural settings that include both living and nonliving matter [1]. The formation of arborized patterns in physical and chemical systems is driven by a variety of processes all of which involve a combination of erosion, transport, and deposition. On the laboratory scale, these processes can involve chemical dissolution of brittle matrices by a penetrating reactive fluid [2,3], advective rearrangement of unconsolidated media, dielectric breakdown of conducting media [4,5], formation of fingerlike protrusions in dense granular suspensions [6], formation of beach rills in natural drainage systems [7,8], etc. On planetary scales, melt transport in the mantle arises via branching morphologies that lead to localized channels of widths up to 100 m [9–11], and water-driven erosion and branching in glaciers arises on scales of the order of 10 m [12]. In biological systems, the best known arborized systems are vasculatures in plants and animals. These arise through morphogenetic mechanisms involving gradients and physical flows that arrange and rearrange matter through a variety of feedback mechanisms at the cellular, organismal, and societal level [13,14]. Examples include slime molds [15], vascular networks [16], and nest architectures of social insects [17].

Models based on porous flow theory [18,19] are capable of describing flow through these branched networks. However, their formation requires nonlinear models with multiple evolving phase boundaries which are still only partially understood both theoretically and experimentally. Here, we propose a simple model via an effective continuum theory that links flow, permeability, and

pressure gradients by considering pore-scale grain dislodgement in a relatively brittle structure. Numerical solutions of the resulting governing equations show the emergence of branching morphologies through selective erosion and subsequent flow enhancement.

Mathematical model.—Our starting point is a fluid-filled porous domain Ω comprised of a rigid grain microstructure with characteristic pore size l , as in the Fig. 1(a) inset. The fluid is of viscosity η and density ρ . On length scales large compared to the pore size $L \gg l$, we can define macroscopic continuum fields that include the solid fraction $\phi(\mathbf{x}, t)$ and volumetric fluid flux $\mathbf{q}(\mathbf{x}, t)$ as averages of microscopic quantities [20]. Pressure gradients over macroscopic lengths $\Gamma \sim |\nabla p|$ drive motion of the interstitial fluid at velocities $V \sim |\mathbf{q}|$ relative to the pore structure. Balancing the pressure gradients and viscous resistance at a scaling level implies that $\Gamma \sim \eta V / l^2$, so that individual grains feel forces of magnitude $\eta V l \sim \Gamma l^3$. When these overcome the attractive forces providing microstructural integrity, grains are dislodged, and the local permeability of the medium evolves. Symmetry arguments introduced in [21] suggest an erosion rate depending on the pressure gradient magnitude as a proxy for pore-scale grain tractions. Denoting the network breaking stress $B(\mathbf{x}, t)$, we write the most general such rate law

$$\partial_t \phi = -e_0 \phi f(|\nabla p|, B/l), \quad (1)$$

where e_0 is an erosion rate and f is a nonnegative dimensionless function that vanishes for $|\nabla p| < B/l$. Our original model [21] accounted for the relative motion

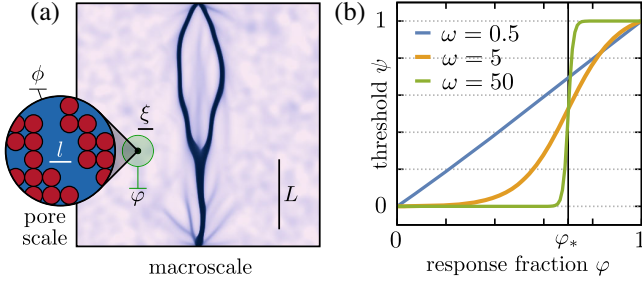


FIG. 1. Schematic of model fields, length scales, and erosion criteria. (a) Branched patterns in porous media can emerge on macroscopic lengths L due to interactions at the pore size l . In this simulated pattern, eroded regions of low solid fraction $\phi(\mathbf{x}, t)$ are blue. At a given point on the macroscale (black dot), ϕ is the fraction of a pore-scale integration volume (inset) occupied by rigid grain microstructure (red circles). Fluid-mediated forces on grains induce stresses over a macroscopic region (shaded green circle) characterized by the communication length ξ . The response fraction φ is the spatial average of ϕ throughout this region. (b) The erosion threshold function $\psi(\varphi) = c_0 \tanh[\omega(\varphi - \varphi_*)] + c_1 \in [0, 1]$ represents resistance to grain dislodgement at response fraction φ .

of the grains, fluid, and static porous medium via a three-phase description allowing dislodged grains to deposit back onto the microstructure. Here, we omit deposition and focus on a simpler two-phase model assuming loose grains to be indistinguishable from fluid.

In terms of a characteristic breaking stress B_0 and time scale $\tau = 1/e_0$, we can define a characteristic length $L = l(B_0/\eta e_0)$ and pressure gradient magnitude $\Gamma = B_0/l$. This allows us to rescale our variables and parameters accordingly; they should be assumed dimensionless for the remainder of the Letter unless otherwise specified. (Please see Supplemental Material (SM) section SM.1 [22] for the full dimensional system of equations.)

Assuming that the solid is relatively stiff but brittle so that it does not deform, the volumetric fluid flux \mathbf{q} is well described by Darcy's law

$$\mathbf{q} = -\kappa(\phi)\nabla p, \quad \kappa(\phi) = \frac{(1-\phi)^3}{\phi^2}, \quad (2)$$

where the dimensionless permeability $\kappa(\phi)$ is the well-known Carman-Kozeny relation [18,19]. Furthermore, if the fluid is incompressible, conservation of mass implies

$$\nabla \cdot \mathbf{q} = -s(\mathbf{x}, t), \quad (3)$$

where $s(\mathbf{x}, t)$ is the rate at which fluid is depleted due to processes such as bulk reaction or evaporation. By combining the previous two equations, \mathbf{q} can be eliminated to obtain an elliptic equation for the pressure,

$$\nabla \cdot [\kappa(\phi)\nabla p] = s. \quad (4)$$

Boundary conditions correspond to specified fluxes q_{in} and q_{out} on boundary regions of inflow $\partial\Omega_{\text{in}}$ and outflow $\partial\Omega_{\text{out}}$ (see SM.2 [22] for details). We note the flow direction, which is determined by the boundary flux and fluid depletion signs, may be reversed with no change to morphogenic pattern formation because the erosion rule (1) is agnostic to the substitution $\nabla p \rightarrow -\nabla p$.

To close the system, we must relate the dimensionless erosion rate f to the fields $\phi(\mathbf{x}, t)$ and $p(\mathbf{x}, t)$. A minimal analytic form for f suggests $f = \max\{0, \nabla p \cdot \nabla p - B^2/l^2\}$. The breaking stress $B(\mathbf{x}, t)$ is itself a nonlocal function of the solid fraction, depending on the grain density within a region of size ξ , a stress communication length which may depend on the porosity. Here, we assume the following hierarchy of constant lengths $l \ll \xi \ll L$, consistent with frangible brittle solids. In this limit, we introduce a simple erosion threshold $B^2/l^2 = \psi(\varphi)$, defining the response fraction $\varphi(\mathbf{x}, t)$ as the convolution of $\phi(\mathbf{x}, t)$ with a Gaussian kernel of length scale ξ , representing a spatial average of the solid fraction as shown in Fig. 1(a) (see SM.3 [22] for details). Thus, the dimensionless form of the erosion rate law (1) becomes

$$\partial_t \phi = -\phi \max\{0, \nabla p \cdot \nabla p - \psi(\varphi)\}. \quad (5)$$

For the functional form of the threshold, we consider a sigmoid $\psi(\varphi) \in [0, 1]$ centered at a critical phase fraction φ_* , where the behavior is roughly linear over a scale $\Delta\varphi \sim 1/\omega$, where ω represents a sharpness parameter as shown in Fig. 1(b). See SM.4 [22] for the exact form. We note that our functional choice satisfies $\psi'(\varphi) > 0$, i.e., the medium becomes more resistant to erosion at larger φ .

Equations (4) and (5) together determine the evolution of the permeability of the porous medium, $\phi(\mathbf{x}, t)$, and the pressure, $p(\mathbf{x}, t)$, once we specify an initial condition. Ignoring anisotropy in grain orientation and packing, we set $\phi(\mathbf{x}, 0) = \phi_0 + \delta\phi(\mathbf{x})$, with ϕ_0 a constant and $\delta\phi$ a perturbed packing structure described as a random Gaussian thermal noise field with zero mean, variance σ_ϕ^2 , and correlation length $\zeta \gg l$ satisfying

$$\langle \delta\phi(\mathbf{x})\delta\phi(\mathbf{y}) \rangle_r = \sigma_\phi^2 \exp(-r/\zeta). \quad (6)$$

Here, $\langle * \rangle_r = \int_\Omega (*) d\mathbf{x} d\mathbf{y} / \text{vol}(\Omega)$ is a spatial average over all $\mathbf{x}, \mathbf{y} \in \Omega$ such that $|\mathbf{x} - \mathbf{y}| = r$.

The correlation length ζ and stress communication length ξ control the characteristic channel width w_c . From (5), loss of solid material at a point reduces resistance to further erosion in a surrounding neighborhood of size ξ —qualitatively similar to descriptions of nonlocal damage accumulation in settings such as hydraulic fracturing [23]. Features in the ϕ field, initially of size ζ , correspond to smoothed features in the φ field. Thus, the channel width scale satisfies $\zeta^2 < w_c^2 < \xi^2 + \zeta^2$, approaching the small limit for large values of the packing variance

σ_ϕ^2 and vice versa, consistent with results obtained using the three-phase model [21]. The width of a given channel scales with w_c and varies with the amount of flux it conducts. See SM.5 [22] for details.

Before considering the spatiotemporal evolution of the flow and permeability, we examine the local dependence of erosion on the threshold shape $\psi(\phi)$ and local flux \mathbf{q} . Letting $\langle * \rangle = \int_A (*) d\mathbf{x} / \text{vol}(A)$ denote a spatial average over a mesoscopic region A , we introduce the scalar fields $\Phi = \langle \phi \rangle$, $G^2 = \langle \nabla p \cdot \nabla p \rangle$, and $Q^2 = \langle \mathbf{q} \cdot \mathbf{q} \rangle$. We see they satisfy $Q = -\kappa(\Phi)G$, derived by averaging (2). Differentiating this relation and combining it with an averaged (5) yields a set of purely time-dependent equations describing trajectories through forcing-response phase space. For eroding states with $G^2 > \psi(\Phi)$,

$$\frac{d\Phi}{dt} = -\Phi(G^2 - \psi), \quad (7a)$$

$$\frac{d(G^2)}{dt} = 2G^2 \left[\left(\frac{\Phi \kappa'}{\kappa} \right) (G^2 - \psi) + \frac{\dot{Q}}{Q} \right]. \quad (7b)$$

Sustained erosion does not occur if $\dot{Q} = 0$, for which points on the threshold surface $G^2 = \psi$ are stable equilibria. Eroding states reach the threshold in finite time, as can be seen from (7a). For $\dot{Q}/Q > 0$, this is not the case. The quantity $\Phi \kappa' / \kappa < 0$ is negative, so the squared gradient decays or grows when the first or second term in (7b), respectively, dominates the other. The majority of the system's evolution takes place along a monotonically increasing slow manifold $G_s(\Phi)$ where the two are balanced, corresponding to $d(G^2)/dt = 0$. From (7b),

$$G_s(G_s^2 - \psi) = \frac{\dot{Q}}{\Phi \kappa'}, \quad (8)$$

a cubic with one real root. In Fig. 2(a), we show the trajectories and slow manifolds for varying \dot{Q} . In Fig. 2(b), we plot the rate of erosion on the manifold, $f_s = G_s^2 - \psi$, for thresholds of varying sharpness at a particular flux rate \dot{Q} . Theoretical bounds $f_0 > f_s > f_1$, corresponding to constant thresholds $\psi = 0$ and 1, are plotted as black lines. Both are monotonically increasing, diverge as $\Phi \rightarrow 1$, and vanish as $\Phi \rightarrow 0$, so the rate of erosion slows over long times. This effect is mitigated by a transition from $f \approx f_1$ to f_0 near $\Phi \approx \varphi_*$. For sharp thresholds of large ω , this effect is dominant and erosion accelerates upon reaching the transition region. The relative difference between the bounding rates, $(f_0 - f_1)/f_1$, vanishes as Φ grows. In particular, when $\varphi < \varphi_{\text{star}}$ erosion is qualitatively faster than when $\varphi > \varphi_{\text{star}}$. See SM.6 [22] for details.

Branching morphospaces.—Now, we turn to the spatiotemporal evolution of the flow and permeability fields in two-dimensional simulations. We aim to understand when, how, and what arborization motifs arise as a

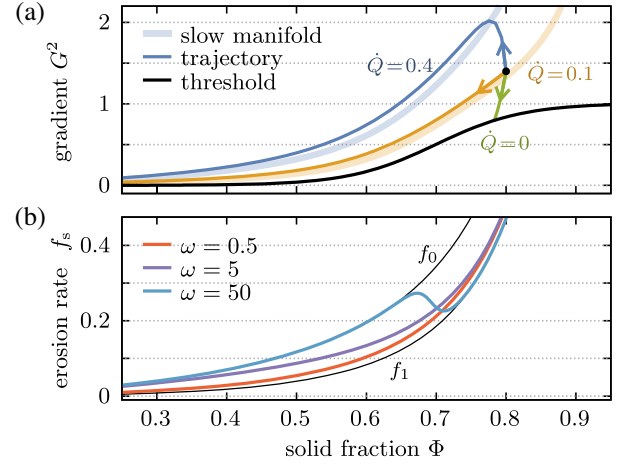


FIG. 2. Homogeneous model of erosion in the presence of an externally controlled flux $Q(t)$ defined by (7). (a) Phase trajectories through forcing-response space with initial condition $(\Phi, G^2) = (0.8, 1.4)$ are shown for varying \dot{Q} . The erosion threshold $\psi(\Phi)$ has $\omega = 8$, $\varphi_* = 0.7$. Constant-flux trajectories reach the threshold quickly, stopping erosion in finite time. For $\dot{Q} \neq 0$, sustained erosion takes place at long times along the slow manifold $G_s^2(\Phi)$, plotted here as a translucent, thick line. (b) The erosion rate along the manifold, $f_s = G_s^2 - \psi$, is plotted for three thresholds with $\varphi_* = 0.7$ and varying sharpness ω , subject to $\dot{Q} = 0.1$. Bounds on the rate $f_0 > f_s > f_1$ are plotted as black lines.

function of the boundary conditions, the dynamical rate of boundary fluxes, and the nature and functional form of the breaking threshold function. We integrate the coupled set of Eqs. (4) and (5) on a square domain $\Omega = [-5, 5]^2 \in \mathbb{R}^2$, employing a second-order forward Euler method with Richardson extrapolation for error estimation and adaptive time stepping [24]. See SM.7 [22] for details. We adopt boundary conditions which ramp up the flux from zero over a duration T . Introducing $r(t) = \min\{1, t/T\}$, we set the fluid depletion rate and boundary fluxes as $s(\mathbf{x}, t) = \hat{s}r(t)$, $q_{\text{in}}(\mathbf{x}, t) = \hat{q}_{\text{in}}r(t)$, $q_{\text{out}}(\mathbf{x}, t) = \hat{q}_{\text{out}}r(t)$, where we have introduced a set of hatted constants corresponding to final magnitudes. This implies a uniform bulk fluid sink \hat{s} evenly distributed throughout the domain. Similarly, the boundary fluxes are assumed to be uniform everywhere on the regions $\partial\Omega_{\text{in}}$ and $\partial\Omega_{\text{out}}$, which we center on the bottom and top walls of the domain, respectively.

There are two feedback mechanisms through which erosion in the model promotes itself. The first, observed in the homogeneous system, is the threshold reduction due to previous erosion. The second is a direct effect of the coupling between flux and permeability. According to (2), flux is preferentially directed along paths of larger permeability, so that, as it grows, flow from other parts of the domain is redistributed to eroded areas. In terms of the homogeneous phase space shown in Fig. 2(a), the resulting flux increase moves quickly eroding areas onto

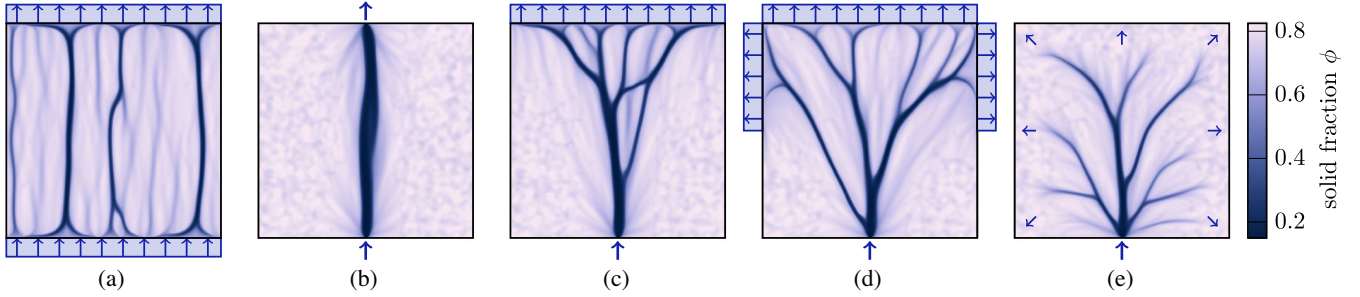


FIG. 3. Erosion patterns as functions of boundary conditions obtained by solving (4) and (5). The solid fraction $\phi(\mathbf{x}, t)$ is shown at $t = 50$. The integrated flux through the system is ramped from zero to a final magnitude $F = \hat{q}_{\text{in}} w_{\text{in}}$ over a duration $T = 10$. Flow enters on the bottom wall and exits through the top wall (a)–(d) or via evaporation in the bulk (e). If the regions of inflow and outflow are of similar size as in (a) and (b), flow is concentrated in straight channels. If they are of different sizes as in (c)–(e), one inflow channel branches into many at the outflow. The boundary widths satisfy $w_{\text{in}} = 0.1$ or 10 ; $w_{\text{out}} = 0.1, 10$ or 20 . Simulation parameters: grid size 1000^2 , $\phi_0 = 0.8$, $\varphi_* = 0.7$, $\sigma_\phi = 0.02$, $\zeta = 0.1$, $\xi = 0.1$, $\omega = 6.5$, $F = 0.8$. (See SM movie 1 [22] for visualizations of the dynamics of arborization that correspond to this figure.)

slow manifolds G_s^2 of higher \dot{Q} , speeding up erosion. Slowly eroding areas experience the opposite effect until so much flow is diverted that $\dot{Q} \leq 0$, so erosion ceases. In this way, flow enhancement leads directly to selective erosion of high- κ channelized regions of width w_c . For a given integrated fluid flux at the boundary F , the number of channels to form in the absence of geometric constraints will scale as $N_c \sim F/w_c$; in what follows, $N_c > 1$.

In Fig. 3, we show the results of simulations with four different combinations of boundary conditions and bulk evaporation rates. In the first four panels Figs. 3(a)–3(d), we set $\hat{s} = 0$ and consider the effect of variation in boundary flux width. Generically, if either the inlet width w_{in} or the outlet width w_{out} are larger than the emergent channel size w_c , boundary fluxes induce the formation of multiple channels, as seen in Fig. 3(a). If both are less than w_c , a single channel is favored as in Fig. 3(b). (We note branching in these settings is possible—Fig. 1(a) shows a single channel split and consolidate—but only given conveniently located low- κ regions of the initial condition in the $\xi \ll \zeta$ limit.) If neither is true, i.e., $w_{\text{in}} < w_c < w_{\text{out}}$, then N_c channels are created at the outlet and one at the inlet, as in Figs. 3(c) and 3(d). In Fig. 3(e), we show the effect of bulk-evaporation driven flow with $\hat{s} > 0$, a single inlet and no outlet. Because the channel width $w_c \ll L$ the system size, multiple channels form in the bulk, although their number and width is attenuated with distance from the inlet. These results may be summarized via a simple geometric argument suggesting a formula for reliable branch generation. If the number of channel heads distributed along the inlet and outlet are not the same, branching junctions arise in their linking, which is favored by flow continuity.

Finally, we consider the effects of varying the form of the erosion threshold function $\psi(\varphi)$, via its sharpness ω , and the rate of flux increase, via the ramp-up time T . Figure 4 shows a grid of eroded patterns corresponding to combinations of these two parameters. Low rates of flux increase

correspond to slow manifolds G_s^2 close to the threshold ψ , so small drops in the pressure gradient can yield $|\nabla p|^2 < \psi$. Conversely, rapidly increasing fluxes induce large pressure gradients $|\nabla p|^2 \gg \psi$ before flow reorganization can occur, leading to large-scale washout. We conclude that $T \gg 1$ is necessary for selective erosion. Increasing ω yields more

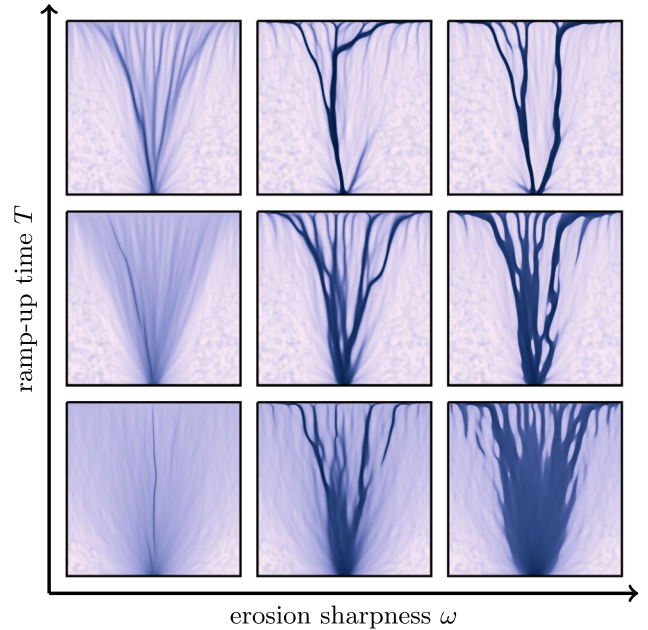


FIG. 4. Erosion patterns as functions of flux dynamics and threshold shape. The solid fraction $\phi(\mathbf{x}, t)$ is plotted with the Fig. 3 color scheme at $t = 50$, subject to varied ramp time T and sharpness ω . Increasing T or ω promotes confinement of erosion to a footprint which is smaller for more slowly increasing fluxes and larger for sharper thresholds. Boundary fluxes: $w_{\text{in}} = 0.5$, $w_{\text{out}} = 10$, $\hat{s} = 0$, $F = 0.5$. Sharpness and ramp duration: $\omega = \{1, 8, 15\}$, $T = \{0, 3, 10\}$. Other parameters: grid size 1024^2 , $\phi_0 = 0.8$, $\varphi_* = 0.7$, $\sigma_\phi = 0.02$, $\zeta = 0.08$, $\xi = 0.05$. (See SM movie 2 [22] for visualizations of the dynamics of arborization that correspond to this figure).

erosion across the domain—consistent with the relationship between the erosion rate and ω as in Fig. 2(b)—and sharper boundaries between eroded and uneroded regions. This relates to qualitatively higher rates of erosion in the region $\varphi < \varphi_*$ corresponding to sharper thresholds. In physical terms, ω represents the immediacy with which a porous material's breaking stress vanishes after a critical amount of erosion. More selectivity in eroding below the critical solid fraction is associated with more rapidly vanishing breaking stresses.

These results are qualitatively similar to observations from the three-phase model [21], which predicted a spectrum of patterns from washout to defined channelization. Adding a mobile grain phase to this work would introduce another avenue for flow enhancement with an independent timescale associated with deposition. The regions of intermediate phase fraction on the left and bottom of Fig. 4 could redirect flow away as pores fill with grains, leading to the concentration of flow in the most-eroded regions and more defined patterns at long times.

Conclusions.—Our minimal continuum model for the coupled dynamics of erosion, flow, and permeability in a porous material shows how complex branching patterns can arise from simple causes. While the model and discussion are rooted in the language of frangible solids, our framework is broadly applicable beyond this setting, to branching patterns generated by local interactions subject to nonlocal flow constraints. Generalizing this to biological settings that feature nonlinear couplings such as that between nutrient concentration and flow behavior, e.g., if portions of solid may be flow-seeking or flow-avoiding [14] is a natural next step.

N. D. was partially supported by the NSF-Simons Center for Mathematical and Statistical Analysis of Biology at Harvard, Grant No. 1764269, and the Harvard Quantitative Biology Initiative. C. H. R. and N. D. were partially supported by the National Science Foundation under Grant No. DMS-1753203. C. H. R. was partially supported by the Applied Mathematics Program of the U.S. DOE Office of Science Advanced Scientific Computing Research under Contract No. DE-AC02-05CH11231. L. M. was partially supported by the National Science Foundation under Grants No. DMR-2011754 and No. DMR-1922321.

N. J. D. and D. C. F. contributed equally to this work.

*Corresponding author.

Lmahadev@g.harvard.edu

- [1] V. Fleury, J.-F. Gouyet, and M. Lonetti, *Branching in Nature: Dynamics and Morphogenesis of Branching Structures, from Cell to River Networks*, Centre de Physique des Houches Vol. 14 (Springer, Berlin, 2001).
- [2] P. Szymczak and A. J. Ladd, *Geophys. Res. Lett.* **38**, 1 (2011).
- [3] P. Grodzki and P. Szymczak, *Phys. Rev. E* **100**, 033108 (2019).
- [4] P. M. Duxbury, P. L. Leath, and P. D. Beale, *Phys. Rev. B* **36**, 367 (1987).
- [5] S. Zapperi, P. Ray, H. E. Stanley, and A. Vespignani, *Phys. Rev. Lett.* **78**, 1408 (1997).
- [6] P. Cerasi and P. Mills, *Phys. Rev. E* **58**, 6051 (1998).
- [7] N. Schorghofer, B. Jensen, A. Kudrolli, and D. H. Rothman, *J. Fluid Mech.* **503**, 357 (2004).
- [8] A. E. Lobkovsky, A. V. Orpe, R. Molloy, A. Kudrolli, and D. H. Rothman, *J. Fluid Mech.* **605**, 47 (2008).
- [9] D. McKenzie, *J. Petrol.* **25**, 713 (1984).
- [10] M. Spiegelman, *J. Fluid Mech.* **247**, 17 (1993).
- [11] M. Spiegelman, P. B. Kelemen, and E. Aharonov, *J. Geophys. Res. Solid Earth* **106**, 2061 (2001).
- [12] I. J. Hewitt, *J. Glaciol.* **57**, 302 (2011).
- [13] S. Camazine, *Self-Organization in Biological Systems* (Princeton University Press, Princeton, NJ, 2001).
- [14] S. A. Ocko and L. Mahadevan, *Phys. Rev. Lett.* **114**, 134501 (2015).
- [15] A. Tero, S. Takagi, T. Saigusa, K. Ito, D. P. Bebber, M. D. Fricker, K. Yumiki, R. Kobayashi, and T. Nakagaki, *Science* **327**, 439 (2010).
- [16] H. Ronellenfitsch and E. Katifori, *Phys. Rev. Lett.* **123**, 248101 (2019).
- [17] A. Khuong, J. Gautrais, A. Perna, C. Sbaï, M. Combe, P. Kuntz, C. Jost, and G. Theraulaz, *Proc. Natl. Acad. Sci. U.S.A.* **113**, 1303 (2016).
- [18] A. E. Scheidegger, *The Physics of Flow through Porous Media*, rev. ed. (Macmillan, New York, 1960).
- [19] J. Bear, *Dynamics of Fluids in Porous Media* (Dover, New York, 1988), p. 764.
- [20] D. Drew and S. Passman, *Theory of Multicomponent Fluids*, Applied Mathematical Sciences Vol. 135 (Springer, New York, 1999).
- [21] A. Mahadevan, A. V. Orpe, A. Kudrolli, and L. Mahadevan, *Europhys. Lett.* **98**, 58003 (2012).
- [22] See Supplemental Material at <http://link.aps.org/supplemental/10.1103/PhysRevLett.125.158002> for derivations, elaborations, descriptions of the numerical solution procedure, and visualizations of the dynamics of arborization shown in Figs. 3 and 4.
- [23] G. I. Barenblatt, M. Bertsch, and C. Nitsch, *Commun. Appl. Math. Comput. Sci.* **1**, 143 (2006).
- [24] M. T. Heath, *Scientific Computing: An Introductory Survey*, McGraw-Hill Series in Computer Science (McGraw-Hill, New York, 1997).

Supplementary Information

Flow-driven branching in a frangible porous medium

Nicholas J. Derr,^{1,*} David C. Fronk,^{2,*} Christoph A. Weber,³
Amala Mahadevan,⁴ Chris H. Rycroft,^{1,5} and L. Mahadevan^{1,2,6}

¹*John A. Paulson School of Engineering and Applied Sciences, Harvard University, Cambridge, MA 02138*

²*Department of Organismic and Evolutionary Biology, Harvard University, Cambridge, MA 02138*

³*Max Planck Institute for the Physics of Complex Systems, Dresden, Germany*

⁴*Woods Hole Oceanographic Institution, Woods Hole, MA 02450*

⁵*Computational Research Division, Lawrence Berkeley National Laboratory, Berkeley, CA 94720*

⁶*Department of Physics, Harvard University, Cambridge, MA 02138*

I. MODEL EQUATIONS

The complete set of dimensional model equations is as follows:

$$\frac{\partial \phi}{\partial t} = - \left(\frac{e_0 l^2}{B_0^2} \right) \phi \max \{0, \nabla p \cdot \nabla p - \psi(\varphi)\}, \quad (1a)$$

$$\mathbf{q} = - \left(\frac{l^2 \kappa(\phi)}{\eta} \right) \nabla p, \quad (1b)$$

$$\psi(\varphi) = \left(\frac{B_0}{l} \right)^2 [c_1 \tan(\omega(\varphi - \varphi_*)) + c_2], \quad (1c)$$

$$\nabla \cdot \left[\left(\frac{l^2 \kappa(\phi)}{\eta} \right) \nabla p \right] = s, \quad (1d)$$

$$\varphi(\mathbf{x}, t) = \int_{\Omega} \frac{\phi(\mathbf{x}', t)}{2\pi\xi^2} \exp\left(-\frac{|\mathbf{x} - \mathbf{x}'|^2}{2\xi^2}\right) d\mathbf{x}'. \quad (1e)$$

Note that c_1 and c_2 are dimensionless constants given in SI.4. As described in the main Letter, we introduce the length, time and pressure gradient scales

$$L = l \left(\frac{B_0}{\eta e_0} \right), \quad \tau = \frac{1}{e_0}, \quad \Gamma = \frac{B_0}{l}, \quad (2)$$

so that we can rescale variables and operators as

$$\mathbf{x} \rightarrow L\tilde{\mathbf{x}}, \quad t \rightarrow \tau\tilde{t}, \quad p \rightarrow \Gamma L\tilde{p}, \quad \psi \rightarrow \Gamma^2\tilde{\psi}, \quad \mathbf{q} \rightarrow \frac{L}{\tau}\tilde{\mathbf{q}}, \quad \nabla \rightarrow L^{-1}\tilde{\nabla}, \quad s \rightarrow \tau^{-1}\tilde{s}, \quad \xi \rightarrow L\tilde{\xi}, \quad (3)$$

where tildes denote dimensionless variables. The full dimensionless model system is given by

$$\frac{\partial \phi}{\partial \tilde{t}} = -\phi \max \{0, \tilde{\nabla} \tilde{p} \cdot \tilde{\nabla} \tilde{p} - \tilde{\psi}(\varphi)\}, \quad (4a)$$

$$\tilde{\mathbf{q}} = -\kappa(\phi) \tilde{\nabla} \tilde{p}, \quad (4b)$$

* N.J.D. and D.C.F. contributed equally to this work.

$$\tilde{\psi}(\varphi) = c_1 \tan(\omega(\varphi - \varphi_*)) + c_2, \quad (4c)$$

$$\tilde{\nabla} \cdot (\kappa(\phi) \tilde{\nabla} \tilde{p}) = \tilde{s}, \quad (4d)$$

$$\varphi(\tilde{\mathbf{x}}, \tilde{t}) = \int_{\Omega} \frac{\phi(\tilde{\mathbf{x}}', \tilde{t})}{2\pi\tilde{\xi}^2} \exp\left(-\frac{|\tilde{\mathbf{x}} - \tilde{\mathbf{x}}'|^2}{2\tilde{\xi}^2}\right) d\tilde{\mathbf{x}}'. \quad (4e)$$

For the remainder of the SI we use the dimensionless relations, omitting tildes.

II. FLUX BOUNDARY CONDITIONS

The pressure distribution $p(\mathbf{x}, t)$ satisfies the constraint

$$\nabla \cdot (\kappa(\phi) \nabla p) = s, \quad (5)$$

where $s(\mathbf{x}, t)$ is the rate of fluid depletion due to effects such as reaction or evaporation. Let the material flux into and out of the system be respectively denoted $q_{\text{in}}(\mathbf{x}, t)$ and $q_{\text{out}}(\mathbf{x}, t)$, where these positive functions are defined on the non-overlapping surfaces $\partial\Omega_{\text{in}}, \partial\Omega_{\text{out}} \in \partial\Omega$. We set

$$\partial_n p = \begin{cases} q_{\text{in}}/\kappa(\phi), & \mathbf{x} \in \partial\Omega_{\text{in}}, \\ -q_{\text{out}}/\kappa(\phi), & \mathbf{x} \in \partial\Omega_{\text{out}}, \\ 0, & \text{otherwise,} \end{cases} \quad (6)$$

where the boundary and bulk material fluxes satisfy

$$\int_{\partial\Omega_{\text{out}}} q_{\text{out}} dS + \int_{\Omega} s dV = \int_{\partial\Omega_{\text{in}}} q_{\text{in}} dS \quad (7)$$

in accordance with the incompressibility condition $\nabla \cdot \mathbf{q} = -s$.

III. RESPONSE FRACTION

The response fraction $\varphi(\mathbf{x}, t)$ represents the spatial average of $\phi(\mathbf{x}', t)$ within a neighborhood of size ξ centered at \mathbf{x} . As we consider two-dimensional systems in the main Letter, we set

$$\varphi(\mathbf{x}, t) = \int_{\Omega} \frac{\phi(\mathbf{x}', t)}{2\pi\xi^2} \exp\left(-\frac{|\mathbf{x} - \mathbf{x}'|^2}{2\xi^2}\right) d\mathbf{x}'. \quad (8)$$

It is necessary to formulate a policy for evaluating the convolution near domain boundaries where the kernel does not integrate to unity. This is discussed in SI.7.c.

IV. EROSION THRESHOLD FUNCTION

The form of the erosion threshold $\psi(\varphi)$ is defined in terms of a sigmoidal function $H(\varphi)$ transitioning from 0 to 1,

$$H(\varphi) = \frac{1}{2} [1 + \tanh(\omega(\varphi - \varphi_*))]. \quad (9a)$$

This function is shifted and scaled to satisfy $\psi(0) = 0$ and $\psi(1) = 1$, so that

$$\psi(\varphi) = \frac{H(\varphi) - H(0)}{H(1) - H(0)}. \quad (9b)$$

The result is a monotonically increasing threshold $\psi(\varphi)$ with the prescribed endpoint values.

V. LENGTH SCALES

The problem specification contains three macroscopic lengths: the noise correlation length ζ , the communication length ξ , and the length scale $L = B_0 l / \eta e_0$, where B_0 is the network breaking stress, l the pore size, η the penetrating fluid viscosity and e_0 the erosion rate. The boundary conditions introduce the inlet and outlet widths w_{in} and w_{out} . In addition, given the fluid throughput $F = q_{\text{in}} w_{\text{in}}$, we can construct a scaling for the number of channels $N_c \sim F/w_c$, where the characteristic channel width w_c is quantified below.

Channel width and branching can largely be understood in terms of ratios of these length scales, plus the packing fraction variance σ_ϕ^2 . Recall from the main Letter that channelization occurs through two feedback loops where 1) flow is redirected along eroding areas as the conductance rises; and 2) erosion occurs more easily in previously eroded areas as the threshold ψ has fallen. Note the length scale over which ψ falls is not the same as that over which erosion occurs: in particular, if a region of length scale X undergoes erosion, the threshold drops over a region of size $\sqrt{X^2 + \xi^2}$. If the redirection of flow in the size X area happens more quickly than the lowering of the threshold in the larger area, the result is a channel of size X ; conversely, if the redirection of flow is slow compared to the threshold drop, the channel size is $\sqrt{X^2 + \xi^2}$.

Flow is redirected faster when erosion is occurring more quickly, and the erosion rate is highest in those locations where the pressure gradient magnitude most exceeds the threshold. In the results presented, boundary fluxes (and therefore the driving pressure gradients) are ramped up from zero. Channels form when the locations of highest pressure gradient reach the threshold $|\nabla p|^2 > \psi$ and begin to erode.

For a given flux \mathbf{q} passing through a solid fraction field $\phi = \phi_0 + \delta\phi$, where $\delta\phi$ represents a perturbation field with variance σ_ϕ^2 , the pressure gradient has a variance which can be roughly described as

$$\sigma_{|\nabla p|}^2 \approx |\mathbf{q}| \left| \frac{d}{d\phi} \frac{1}{\kappa} \right|^2 \sigma_\phi^2. \quad (10)$$

If $\sigma_{|\nabla p|}$ is not large (we will quantify the comparison shortly), then the high-gradient locations will reach the threshold very shortly before other locations in the domain; there will be insufficient time to begin redirecting flow to the initially eroding locations before the whole domain exceeds the threshold and washout occurs. On the other hand, if $\sigma_{|\nabla p|}$ is large, erosion in the high-gradient locations will begin reorganizing flow well before the rest of the domain reaches the threshold, if in fact it does at all. As such, we link $\sigma_{|\nabla p|}$ and σ_ϕ by scaling the above relation and assume $\sigma_{|\nabla p|} \gg 1$ corresponds to fast initial erosion. We identify the characteristic channel width as approaching the following limits,

$$w_c \sim \begin{cases} \zeta & \text{if } \sigma_\phi \gg (1 - \phi_0)^3 / \hat{q}_{\text{in}} \phi_0, \\ \sqrt{\zeta^2 + \xi^2} & \text{otherwise,} \end{cases} \quad (11)$$

such that fast erosion corresponds to the case where flow reorganization occurs so quickly that it is agnostic to changes in the threshold ψ .

Now, given w_c , comparisons can be made to w_{in} , w_{out} , and the system size. Within the main Letter, we argue that if $w_c > w_{\text{in}}$ but $w_c < w_{\text{out}}$, the system will favor the formation of N_c channels leading to the outlet and a single channel at the inlet. Continuity of flow requires these channels connect to one another; consequentially, the single inlet will branch into the multiple outlets. This can be generalized to the no-outlet case (i.e. where fluid exits the system via bulk effects such as evaporation) by considering the system size an effective w_{out} . Finally, we will note that if ζ or ξ approach the system size, or σ_ϕ approaches zero, the system is effectively homogeneous. We performed simulations to verify this analysis, and the effects of individually varying ζ , ξ , σ_ϕ , and F can be seen in Fig. 1, showing for each parameter p a set of four patterns for increasing or decreasing p .

VI. HOMOGENEOUS MODEL

In the main Letter, we consider a simplified model consisting of homogeneous solid fraction Φ , pressure gradient G , and externally specified flux Q . The governing equations consist of a spatially averaged erosion rate law and Darcy relation,

$$\frac{d\Phi}{dt} = -\Phi \max \{0, G^2 - \psi(\Phi)\}, \quad (12a)$$

$$Q = -\kappa(\Phi)G. \quad (12b)$$

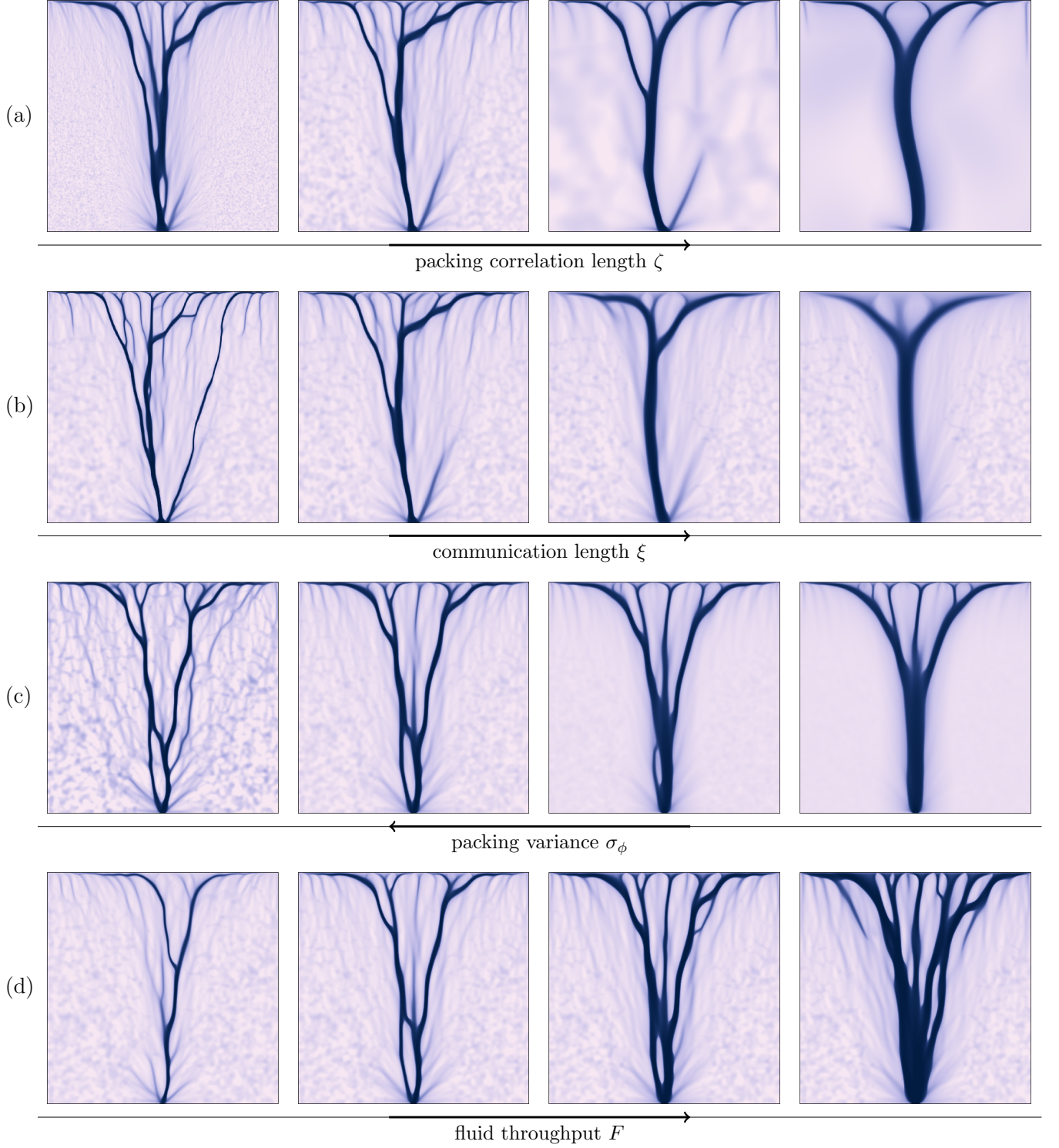


FIG. 1. Examples of pattern formation at $t = 50$ after a ramp-up time $T = 10$ are shown for four varied parameters. The initial conditions of the various simulations may be compared by examining uneroded areas in the domain. The solid fraction $\phi(\mathbf{x}, t)$ is plotted using the color scheme from Fig. 3 in the main Letter. (a) Patterns generated with noise correlation lengths $\zeta = \{0.02, 0.08, 0.32, 0.64\}$. (b) Patterns generated with communication lengths $\xi = \{0.025, 0.05, 0.1, 0.2\}$. (c) Patterns generated with packing variances $\sigma_\phi = \{0.056, 0.018, 0.0056, 0.0018\}$. (d) Patterns generated with fluid throughputs $F = \{0.2, 0.5, 1, 2\}$. Default parameters are $\xi = 0.05$, $\zeta = 0.15$, $\sigma_\phi = 0.02$, $\omega = 8$, $\varphi_* = 0.8$, $\phi_0 = 0.8$, $F = 0.5$. Grid size is 1024^2 for panels (a,b) and 2000^2 for panels (c,d).

The latter relation can be squared and explicitly differentiated to find the rate-of-change of G^2 ,

$$\frac{d(G^2)}{dt} = 2G^2 \left[\left(\frac{\Phi \kappa'}{\kappa} \right) \max \{0, G^2 - \psi\} + \frac{\dot{Q}}{Q} \right], \quad (12c)$$

where we've neglected the Φ -dependence of κ and ψ in the above. Together, (12a) and (12c) define trajectories through the forcing-response space defined by $(\Phi, G^2) \in (0, 1) \times [0, \infty)$. This space can be divided into two regions: a “lower” region $G^2 < \psi$, where pressure gradients are not high enough to induce grain dislodgement and erosion is not occurring, and a “higher” region where $G^2 > \psi$ and material is eroding. In the case of the former,

$$\frac{d\Phi}{dt} = 0, \quad \frac{d(G^2)}{dt} = 2G^2 \frac{\dot{Q}}{Q}, \quad (13)$$

that is, the solid fraction is frozen and the gradient magnitude depends solely on any change in relative flux. In the eroding region, we can drop the max formulation and write

$$\frac{d\Phi}{dt} = -\phi(G^2 - \psi), \quad \frac{d(G^2)}{dt} = 2G^2 \left[\frac{\Phi \kappa'}{\kappa} (G^2 - \psi) + \frac{\dot{Q}}{Q} \right], \quad (14)$$

or, substituting for $\kappa(\Phi)$,

$$\frac{d\Phi}{dt} = -\phi(G^2 - \psi), \quad \frac{d(G^2)}{dt} = 2G^2 \left[-\left(\frac{2 + \Phi}{1 - \Phi} \right) (G^2 - \psi) + \frac{\dot{Q}}{Q} \right], \quad (15)$$

Both the solid fraction Φ and pressure gradient magnitude G^2 evolve in an exponential fashion. As described in the derivation of the erosion rate law, the solid fraction decays with rate $f = G^2 - \psi$; this process leads in turn to exponential decay in the gradient magnitude. If $\dot{Q}/Q > 0$, however, this decay is opposed—and, near $G^2 \approx \psi$, overcome—by growth driven by the increasing flux. The magnitude G^2 is driven by these factors towards a slow manifold G_s^2 described to leading order by $dG/dt = 0$,

$$G_s(G_s^2 - \psi) = \frac{\dot{Q}}{\phi \kappa'} = -\frac{\dot{Q} \Phi^2}{(1 - \Phi)^2 (2 + \Phi)}, \quad (16)$$

which, for $h = \dot{Q}/\phi \kappa'$, has the real root

$$|G_s| = \frac{\psi}{3F} + F, \quad F = \left(\frac{1}{2} \left(h + \sqrt{h^2 - \frac{1}{2} \left(\frac{2\psi}{3} \right)^3} \right) \right)^{1/3}. \quad (17)$$

Note this also provides an analytical representation of the erosion rate along the slow manifold $f_s = G_s^2 - \psi$,

$$f_s = \left(\frac{\psi}{3F} \right)^2 - \frac{\psi}{3} + F^2. \quad (18)$$

These expressions are used to generate the slow manifolds and manifold erosion rates plotted in Fig. 2 in the main Letter. As illustrated in Fig. 2(b), the erosion rate f_s transitions between two limiting functions f_0 for $\psi \approx 0$ and f_1 for $\psi \approx 1$, which can be calculated by substituting the appropriate threshold value in the expressions above. The erosion rate is strictly positive, although since $f_1 < f_0$, there are portions of the parameter space where $f'_s < 0$ near the transition point φ_* .

While the rate is not monotonically increasing with Φ , the gradient magnitude $|G_s|$ is. This can be seen by explicitly differentiating (16) to find

$$\frac{d|G_s|}{d\Phi} = \frac{h' + |G_s| \psi'}{2G_s^2 + f_s}, \quad (19)$$

where $h' = dh/d\Phi$ and $\psi' = d\psi/d\Phi$. The denominator and each term in the numerator are strictly positive.

Now, we consider approximate representations of the slow manifold in limits of Φ . First, note there is significant asymmetry in behavior at low and high solid fraction. As $\Phi \rightarrow 1$, the RHS of (16) diverges, leading to large pressure gradients $G_s^2 \gg \psi$, so that

$$G_s^2 \sim \left(\frac{\dot{Q}}{3}\right)^{2/3} (1 - \Phi)^{-4/3}. \quad (20)$$

Large solid fractions correspond to a regime where the effect of the erosion threshold is unimportant.

Conversely, at small Φ the RHS vanishes, indicating G^2 approaches 0 or ψ (or both.) We will consider a few different cases depending on the behavior of $\psi(\Phi)$ as $\Phi \rightarrow 0$. In each, we will seek an approximate relation between G^2 , \dot{Q} , and Φ . Since (12a) indicates $1/t \sim f$, we can use this to relate the solid fraction and time to obtain the asymptotic rate with which $\Phi \rightarrow 0$. We will see this takes the form $\Phi \sim K_0(\dot{Q}t)^{-K_1}$ for $K_1 > 0$ in general, indicating the solid fraction falls off inversely with increasing flux, with the exponent a function of the threshold behavior at low Φ . Here, we will consider three possible threshold behaviors: approaching a constant ($\psi \sim g^2$, although this case is not considered in the main Letter), linearly approaching zero ($\psi \sim c \Phi$), and being effectively zero ($\psi \sim 0$). Intuition suggests this listing should correspond to an ordering of slowest to fastest rates of erosion, based on the lessening of the threshold.

First, we consider $\psi(0) = g^2$. In the limit as $\Phi \rightarrow 0$, the relation (16) approaches

$$\psi \approx g^2 \implies f_s = G_s^2 - g^2 = \frac{\dot{Q}}{2g} \Phi^2 \implies \Phi \sim g^{1/2} (\dot{Q}t)^{-1/2}, \quad (21)$$

which follows from (12b). (Note that here and in the following examples, the expressions are truncated to leading order in f/ψ .) If $\psi(0) = 0$, but—because ω is not large— $\psi'(0) = c$ for some finite value c (i.e. $c \ll 1$), then (16) approaches

$$\psi \approx c \Phi \implies f_s = G_s^2 - c\Phi = \frac{\dot{Q}}{2\sqrt{c}} \Phi^{3/2} \implies \Phi \sim c^{1/3} (\dot{Q}t)^{-2/3}. \quad (22)$$

Finally, if ω is large so that $\psi \approx 0$ for $\Phi < \varphi_*$, then $f \approx G^2$ so that

$$\psi \approx 0 \implies f_s = G_s^2 = \left(\frac{\dot{Q}\Phi^2}{2}\right)^{2/3} \implies \Phi \sim \dot{Q}^{1/4} (\dot{Q}t)^{-3/4}. \quad (23)$$

This confirms our suspected ordering of the erosion speeds. Moreover, it indicates that long-term erosion is qualitatively different for threshold functions with small ω (i.e. those that smoothly transition from 0 to 1 over $\Phi \in [0, 1]$) and large ω (i.e. switchlike functions where for $\Phi < \varphi_*$ there is essentially no resistance to erosion.) While both depend at long times on the total flux $\dot{Q}t$, the sharp case dies off faster. In addition, for the small ω case, the flux increase rate \dot{Q} plays no role in scaling the response outside of its presence in the flux $\dot{Q}t$.

We now consider the dependence of G_s^2 on the shape of ψ , in particular the effect of changing the sharpness ω . As above, we shall see that lower thresholds correspond to faster erosion rates, suggesting that sharper thresholds yield faster erosion for $\Phi < \varphi_*$ and slower for $\Phi > \varphi_*$. However, because the magnitude of f vanishes and diverges for Φ near 0 and 1, respectively, we shall see the increase in rate at lower solid fractions tends to be of larger consequence than the decrease at larger fractions. As before, we will consider evolution of the system on the slow manifold G_s^2 and the corresponding erosion rate f_s . With this understood, we will neglect the “s” subscript in the following.

Consider an infinitesimal perturbation $\delta\psi(\Phi)$ of a threshold function $\psi_0(\Phi)$ so that $\psi = \psi_0(\Phi) + \delta\psi(\Phi)$, with $\delta\psi(0) = \delta\psi(1) = 0$. The resulting erosion rate is $f(\Phi) = f_0(\Phi) + \delta f(\Phi)$, where $f_0(\Phi)$ is the rate corresponding to ψ_0 as in (18). Omitting the Φ -dependence of functions and rewriting (16) as

$$f\sqrt{f + \psi} = -\frac{\dot{Q}}{\Phi\kappa'}, \quad (24)$$

linearizing yields the relationship

$$\frac{\delta f}{f_0} = -\frac{\delta\psi}{2G_0^2 + f_0}, \quad (25)$$

so that, as predicted, higher(*lower*) thresholds yield lower(*higher*) rates of erosion.

With the form of $\psi(\Phi)$ specified in SI.4, changing the sharpness parameter ω corresponds to a threshold increment

$$\delta\psi = [c_0(\Phi - \varphi_*)\text{sech}^2[\omega_0(\Phi - \varphi_*)]]\delta\omega + \dots, \quad (26)$$

for $c_0 = [H(1) - H(0)]^{-1}$ and where we have neglected correction terms near $\Phi \approx 0, 1$ enforcing $\psi(0) = 0$, $\psi(1) = 1$. Note the leading-order perturbation has odd symmetry about φ_* , such that

$$\delta\psi < 0 \text{ for } \Phi < \varphi_*, \quad \delta\psi > 0 \text{ for } \Phi > \varphi_*. \quad (27)$$

We can quantify the relative importance of these two effects by considering the quantity in the denominator, $D(\Phi) = 2G_0^2 + f_0$, which can be shown to increase monotonically. Recall from (19) that $G'_0 > 0$. Accordingly, $D' < 0$ iff $\psi' > 6G_0G'_0$. Substituting for $f_0 = G_0^2 - \psi_0$ and from (19) shows

$$6G_0G'_0 = \frac{6G_0^2}{3G_0^2 - \psi} \left(\frac{h'}{G_0} + \psi' \right), \quad (28)$$

so we have

$$D' < 0 \quad \text{iff} \quad 0 > \left(\frac{6G_0^2}{3G_0^2 - \psi} \right) h' + \left(\frac{3G_0^2 + \psi}{3G_0^2 - \psi} \right) \psi', \quad (29)$$

but this is impossible, as both terms above are strictly positive. We conclude $D' > 0$ for all Φ .

In regards to (25), this shows that while a sharper threshold yields faster and slower erosion at various solid fractions, the contributions at smaller Φ induce a larger relative change in the rate than those at large Φ . For some duration of erosion T , let Φ_f denote the final solid fraction of some system with initial fraction Φ_0 , so that

$$\Phi_f - \Phi_0 = \int_0^T -\Phi(t)f dt. \quad (30)$$

The perturbed system has an altered erosion rate, so that if its solid fraction at $t = T$ is $\Phi_f + \delta\Phi_f$,

$$\Phi_f + \delta\Phi_f - \Phi_0 = \int_0^T -\Phi(t)[f_0(\Phi) + \delta f(\Phi)]dt, \quad (31)$$

but using $d\Phi = -\Phi f_0 dt$, we can change variables and use the unperturbed solid fraction as a proxy for time,

$$\delta\Phi_f = \int_{\Phi_0}^{\Phi_f} -\left(\frac{\delta f}{f_0} \right) d\Phi = \int_{\Phi_0}^{\Phi_f} \left(\frac{\delta\psi}{2G_0^2 + f_0} \right) d\Phi. \quad (32)$$

Recall that $\delta\psi/\delta\omega$ is odd about φ_* , but $2G_0^2 + f_0$ is monotonically increasing. For long periods of erosion where $\Phi_f \rightarrow 0$, increased sharpness must yield faster erosion if $\varphi_* > 1/2$.

VII. NUMERICAL APPROACH

The full set of model equations,

$$\frac{\partial\phi}{\partial t} = -\phi \max \{0, |\nabla p|^2 - \psi(\varphi)\}, \quad (33a)$$

$$\nabla \cdot (\kappa(\phi)\nabla p) = s, \quad (33b)$$

$$\varphi(\mathbf{x}) = \int_V \frac{\phi(\mathbf{x}')}{2\pi\xi^2} \exp \left[-\frac{|\mathbf{x}' - \mathbf{x}|^2}{2\xi^2} \right] dV. \quad (33c)$$

was simulated with a custom code written in C++ that uses the OpenMP library for multithreading. Equation (33a) is time-integrated using a forward Euler finite-difference method. The elliptic partial differential equation for pressure (33b) is discretized using the finite-element method.

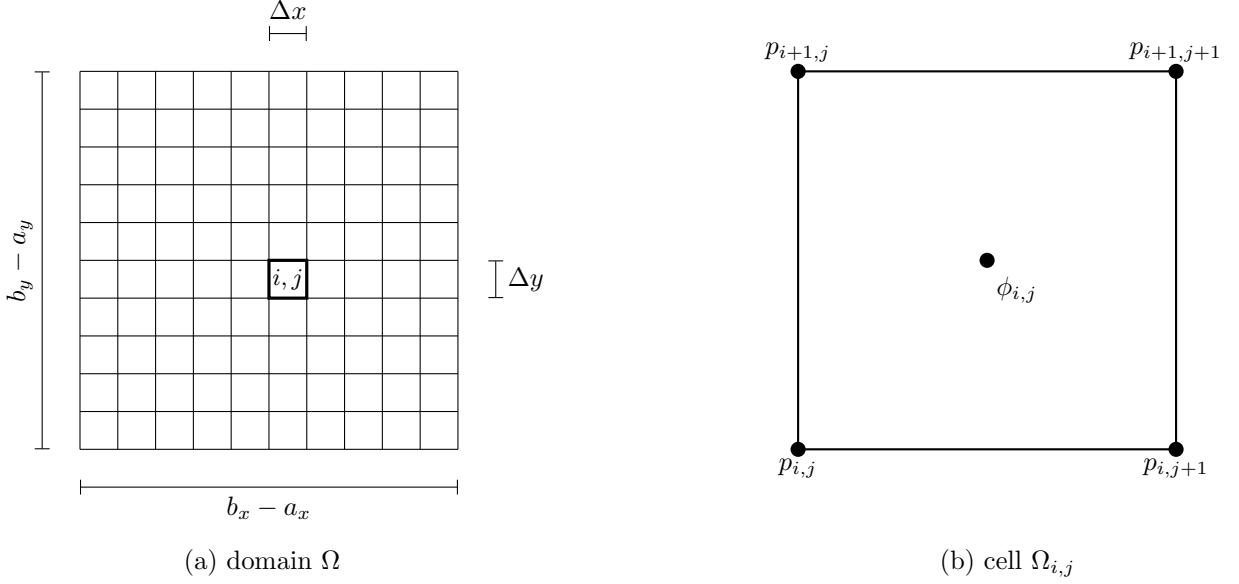


FIG. 2. (a) A diagram of the simulation, where the domain of size $L_x \times L_y$ is divided into a grid of $m \times n$ rectangular cells with dimensions $\Delta x \times \Delta y$. A particular grid cell is indexed as (i, j) . (b) Arrangement of the simulation fields in a grid cell, with the solid fraction ϕ located at the cell center and the pressure located at the cell corners.

a. Grid discretization The domain $\Omega = [a_x, b_x] \times [a_y, b_y]$ can be divided into a regular $m \times n$ grid of rectangular cells of size $\Delta x \times \Delta y$, where

$$\Delta x = \frac{b_x - a_x}{m}, \quad \Delta y = \frac{b_y - a_y}{n}, \quad (34)$$

as seen in Fig. 2. We denote the (i, j) th cell (indexing from 0) as $\Omega_{i,j}$. Its bottom left corner is located at the position

$$\mathbf{c}_{i,j} = (a_x + i\Delta x) \hat{\mathbf{x}} + (a_y + j\Delta y) \hat{\mathbf{y}}, \quad (35)$$

and its center at the position

$$\mathbf{x}_{i,j} = \mathbf{c}_{i,j} + \frac{1}{2} (\Delta x \hat{\mathbf{x}} + \Delta y \hat{\mathbf{y}}). \quad (36)$$

The solid fraction and pressure fields are discretized at the cell center and corner, respectively, so that

$$\phi_{i,j} = \phi(\mathbf{x}_{i,j}, t), \quad p_{i,j} = p(\mathbf{c}_{i,j}, t). \quad (37)$$

Consider the rectangle interior. On the (i, j) th cell, we introduce the coordinates X and Y , defined as

$$X = \frac{x - \mathbf{c}_{i,j} \cdot \hat{\mathbf{x}}}{\Delta x}, \quad Y = \frac{y - \mathbf{c}_{i,j} \cdot \hat{\mathbf{y}}}{\Delta y}, \quad (38)$$

so that the four points corresponding to $X = 0, 1$ and $Y = 0, 1$ represent the rectangle's corners. Let $\mathbf{X} = X\hat{\mathbf{x}} + Y\hat{\mathbf{y}}$. We let $\phi(\mathbf{X}) = \phi_{i,j}$, so that the solid fraction is constant over cell interiors. For the pressure distribution, we introduce four bilinear basis functions $\psi^{(0,0)}$, $\psi^{(0,1)}$, $\psi^{(1,0)}$, and $\psi^{(1,1)}$, satisfying

$$\psi^{k,l}(\mathbf{X}) = \begin{cases} 1 & \text{if } X = k \text{ and } Y = l, \\ 0 & \text{otherwise,} \end{cases} \quad (39)$$

given by

$$\psi^{(0,0)} = (1 - X)(1 - Y), \quad (40a)$$

$$\psi^{(0,1)} = (1 - X)Y, \quad (40b)$$

$$\psi^{(1,0)} = X(1 - Y), \quad (40c)$$

$$\psi^{(1,1)} = XY. \quad (40d)$$

Within cell (i, j) we describe the pressure as a weighted linear combination of the basis functions,

$$p(\mathbf{X}) = \sum_{k=0}^1 \sum_{l=0}^1 p_{i+k, j+l} \psi^{(k, l)}(\mathbf{X}). \quad (41)$$

Moving to a view of the whole domain (and substituting \mathbf{x} for \mathbf{X} accordingly), we introduce global basis functions $\psi_{i,j}(\mathbf{x})$ defined everywhere as

$$\psi_{i,j}(\mathbf{x}) = \begin{cases} \psi^{(0,0)}(\mathbf{x}) & \text{if } \mathbf{x} \in \text{cell } (i, j), \\ \psi^{(0,1)}(\mathbf{x}) & \text{if } \mathbf{x} \in \text{cell } (i, j-1), \\ \psi^{(1,0)}(\mathbf{x}) & \text{if } \mathbf{x} \in \text{cell } (i-1, j), \\ \psi^{(1,1)}(\mathbf{x}) & \text{if } \mathbf{x} \in \text{cell } (i-1, j-1), \\ 0 & \text{otherwise.} \end{cases} \quad (42)$$

The pressure distribution everywhere is then given by a weighted sum over the global basis,

$$p(\mathbf{x}) = \sum_{i,j} p_{i,j} \psi_{i,j}(\mathbf{x}). \quad (43)$$

b. Pressure calculation Given a solid fraction field $\phi_{i,j}$, the finite-element method is used to calculate the corresponding pressure distribution $p_{i,j}$ satisfying (33b). We begin by considering continuum fields $\phi(\mathbf{x})$ and $p(\mathbf{x})$. Multiplying the elliptic constraint (33b) by a scalar test function v and integrating by parts yields a weak form of the relation,

$$\int_{\Omega} \kappa(\phi) \nabla v \cdot \nabla p \, dV = - \int_{\Omega} v s \, dV - \int_{\partial\Omega_{\text{out}}} v q_{\text{out}} dS + \int_{\partial\Omega_{\text{in}}} v q_{\text{in}} dS. \quad (44)$$

Describing the test function as $v(\mathbf{x}) = \sum_{i,j} v_{i,j} \psi_{i,j}(\mathbf{x})$, (44) simplifies to

$$v_{i,j} \left[\int_{\Omega} \kappa(\phi) \nabla \psi_{i,j} \cdot \nabla \psi_{k,l} \, dV \right] p_{k,l} = -v_{i,j} \left[\int_{\Omega} s \psi_{i,j} \, dV \right] - v_{i,j} \left[\int_{\partial\Omega_{\text{out}}} q_{\text{out}} \psi_{i,j} dS \right] + v_{i,j} \left[\int_{\partial\Omega_{\text{in}}} q_{\text{in}} \psi_{i,j} dS \right]. \quad (45)$$

We introduce Greek indices to refer to an individual corner node, i.e. node (i, j) may be referred to as node α . Then the vector of node values p_{α} is described by the linear system

$$M_{\alpha\beta} p_{\beta} = b_{\alpha}, \quad (46a)$$

where the mass matrix $M_{\alpha\beta}$ is

$$M_{\alpha\beta} = \int_{\Omega} \kappa(\phi) \nabla \psi_{\alpha} \cdot \nabla \psi_{\beta} \, dV, \quad (46b)$$

and the source vector b_{α} can be decomposed into three contributions from fluid entering the system through the boundary, exiting the system through the boundary, and exiting the system through the bulk, so that

$$b_{\alpha} = b_{\alpha}^{\text{in}} + b_{\alpha}^{\text{out}} + b_{\alpha}^{\text{bulk}}, \quad (46c)$$

where

$$b_{\alpha}^{\text{in}} = \int_{\partial\Omega_{\text{in}}} q_{\text{in}} \psi_{\alpha} \, dS, \quad b_{\alpha}^{\text{out}} = - \int_{\partial\Omega_{\text{out}}} q_{\text{out}} \psi_{\alpha} \, dS, \quad b_{\alpha}^{\text{bulk}} = - \int_{\Omega} s \psi_{\alpha} \, dV, \quad (46d)$$

respectively. The integral in (46b) can be decomposed into a sum of integrals over each cell,

$$M_{\alpha\beta} = \sum_{i=0}^{m-1} \sum_{j=0}^{n-1} \kappa(\phi_{i,j}) \int_{\Omega_{i,j}} \nabla \psi_{\alpha} \cdot \nabla \psi_{\beta} dV, \quad (47)$$

and these integrals vanish unless nodes α and β are corners on the same cell $\Omega_{i,j}$. As such, the connectivity of the matrix is completely captured by a 3×3 two-dimensional stencil which we can calculate for arbitrary $\phi_{i,j}$. Consider a

single pressure node $p_\alpha = p_{i,j}$. Denoting the constant values of the conductivity $\kappa(\phi)$ over the four neighboring cells as

$$\kappa^{\text{ul}} = \kappa(\phi_{i-1,j}), \quad \kappa^{\text{ur}} = \kappa(\phi_{i,j}), \quad \kappa^{\text{dl}} = \kappa(\phi_{i-1,j-1}), \quad \kappa^{\text{dr}} = \kappa(\phi_{i,j-1}), \quad (48)$$

and introducing the geometric quantities

$$f_{\text{m}} = \frac{1}{3} \left(\frac{\Delta x}{\Delta y} + \frac{\Delta y}{\Delta x} \right), \quad f_{\text{c}} = -\frac{1}{6} \left(\frac{\Delta x}{\Delta y} + \frac{\Delta y}{\Delta x} \right), \quad f_{\text{x}} = \frac{1}{6} \left(\frac{\Delta x}{\Delta y} - 2 \frac{\Delta y}{\Delta x} \right), \quad f_{\text{y}} = \frac{1}{6} \left(\frac{\Delta y}{\Delta x} - 2 \frac{\Delta x}{\Delta y} \right), \quad (49)$$

the 2D stencil representing the matrix row $M_{\alpha\beta}$ is

$$\begin{pmatrix} s_{\text{ul}} & s_{\text{uc}} & s_{\text{ur}} \\ s_{\text{cl}} & s_{\text{cc}} & s_{\text{cr}} \\ s_{\text{dl}} & s_{\text{dc}} & s_{\text{dr}} \end{pmatrix} = \kappa^{\text{ul}} \begin{pmatrix} f_{\text{c}} & f_{\text{y}} & 0 \\ f_{\text{x}} & f_{\text{m}} & 0 \\ 0 & 0 & 0 \end{pmatrix} + \kappa^{\text{ur}} \begin{pmatrix} 0 & f_{\text{y}} & f_{\text{c}} \\ 0 & f_{\text{m}} & f_{\text{x}} \\ 0 & 0 & 0 \end{pmatrix} + \kappa^{\text{dl}} \begin{pmatrix} 0 & 0 & 0 \\ f_{\text{x}} & f_{\text{m}} & 0 \\ f_{\text{c}} & f_{\text{y}} & 0 \end{pmatrix} + \kappa^{\text{dr}} \begin{pmatrix} 0 & 0 & 0 \\ 0 & f_{\text{m}} & f_{\text{x}} \\ 0 & f_{\text{y}} & f_{\text{c}} \end{pmatrix}. \quad (50)$$

If the grid spacing is isotropic and $\Delta x = \Delta y$, this reduces to

$$\begin{pmatrix} s_{\text{ul}} & s_{\text{uc}} & s_{\text{ur}} \\ s_{\text{cl}} & s_{\text{cc}} & s_{\text{cr}} \\ s_{\text{dl}} & s_{\text{dc}} & s_{\text{dr}} \end{pmatrix} = \frac{\kappa^{\text{ul}}}{6} \begin{pmatrix} -2 & -1 & 0 \\ -1 & 4 & 0 \\ 0 & 0 & 0 \end{pmatrix} + \frac{\kappa^{\text{ur}}}{6} \begin{pmatrix} 0 & -1 & -2 \\ 0 & 4 & -1 \\ 0 & 0 & 0 \end{pmatrix} + \frac{\kappa^{\text{dl}}}{6} \begin{pmatrix} 0 & 0 & 0 \\ -1 & 4 & 0 \\ -2 & -1 & 0 \end{pmatrix} + \frac{\kappa^{\text{dr}}}{6} \begin{pmatrix} 0 & 0 & 0 \\ 0 & 4 & -1 \\ 0 & -1 & -2 \end{pmatrix}. \quad (51)$$

For a homogeneous solid fraction, this represents a weighted average of two five-point Laplacian stencils at an angle of 45° from each other.

We can similarly calculate elements of the source vector b_α . Given the assumptions that q_{in} and q_{out} are constant and that the inlet and outlet $\partial\Omega_{\text{in}}$ and $\partial\Omega_{\text{out}}$ have endpoints which coincide with cell corners, we can calculate the first two integrals in (46d) as

$$b_\alpha^{\text{in}} = \begin{cases} q_{\text{in}}\Delta s & \text{if } \alpha \text{ is an interior point of } \partial\Omega_{\text{in}}, \\ q_{\text{in}}\Delta s/2 & \text{if } \alpha \text{ is an endpoint of } \partial\Omega_{\text{in}}, \\ 0 & \text{otherwise.} \end{cases} \quad b_\alpha^{\text{out}} = \begin{cases} -q_{\text{out}}\Delta s & \text{if } \alpha \text{ is an interior point of } \partial\Omega_{\text{out}}, \\ -q_{\text{out}}\Delta s/2 & \text{if } \alpha \text{ is an endpoint of } \partial\Omega_{\text{out}}, \\ 0 & \text{otherwise.} \end{cases} \quad (52)$$

Finally, by assuming s is constant as well, we can calculate the bulk contributions to the source vector,

$$b_\alpha^{\text{bulk}} = \begin{cases} -s\Delta x\Delta y & \text{if } \alpha \text{ is an interior point of } \Omega, \\ -s\Delta x\Delta y/2 & \text{if } \alpha \text{ is a non-corner point of } \partial\Omega, \\ -s\Delta x\Delta y/4 & \text{if } \alpha \text{ is a corner point of } \partial\Omega. \end{cases} \quad (53)$$

The symmetry and diagonal dominance of $M_{\alpha\beta}$ are well suited for solution via the multigrid method; the results presented in the main text were obtained using **tgmg**, a templated implementation of the geometric multigrid method written in C++ and developed by the Rycroft group.

c. Spatial averaging The erosion rate equation (33a) depends not on ϕ but φ , defined in (33c) and reprinted here:

$$\varphi(\mathbf{x}) = \int_V \frac{\phi(\mathbf{x}')}{2\pi\xi^2} \exp\left[-\frac{|\mathbf{x}' - \mathbf{x}|^2}{2\xi^2}\right] dV. \quad (33c)$$

Since the exponential kernel is separable, this can be re-written for $\mathbf{x} = x\hat{\mathbf{x}} + y\hat{\mathbf{y}}$ and $\phi(\mathbf{x}) = \phi(x, y)$ as a series of two convolutions,

$$\phi^{(x)}(y) = \int_{a_x}^{b_x} \frac{\phi(x', y)}{\sqrt{2\pi}\xi} \exp\left[-\frac{|x' - x|^2}{2\xi^2}\right] dx. \quad (54a)$$

$$\varphi(x, y) = \int_{a_y}^{b_y} \frac{\phi^{(x)}(y')}{\sqrt{2\pi}\xi} \exp\left[-\frac{|y' - y|^2}{2\xi^2}\right] dy. \quad (54b)$$

This calculation was performed numerically by performing two one-dimensional discrete convolutions with kernels including neighboring grid points up to a distance 3ξ . We introduce kernels k_i^x and k_j^y with

$$k_i^x = c_x \exp\left[-\frac{(i\Delta x)^2}{2\xi^2}\right], \quad k_j^y = c_y \exp\left[-\frac{(j\Delta y)^2}{2\xi^2}\right], \quad (55)$$

where c_x and c_y are constants. The kernels are subject to the index bounds $-M \leq i \leq M$ and $-N \leq j \leq N$, with

$$M = \left\lfloor \frac{3\xi}{\Delta x} \right\rfloor, \quad N = \left\lfloor \frac{3\xi}{\Delta y} \right\rfloor, \quad (56)$$

and c_x and c_y are chosen to satisfy

$$\sum_{i=-M}^M k_i^x = \sum_{j=-N}^N k_j^y = 1. \quad (57)$$

The discrete analogues of (54a) and (54b) are therefore

$$\phi_j^{(i)} = \sum_{l=-M}^M k_l^x \phi_{i+l,j}, \quad \varphi_{i,j} = \sum_{l=-N}^N k_l^y \phi_{j+l}^{(i)}, \quad (58)$$

and this latter value can be used in the time-integration of $\phi_{i,j}$.

It remains to specify the treatment of the convolution at the boundary, i.e. the value of $\phi_{i,j}$ and $\phi_j^{(i)}$ in the previous line for the out-of-bounds values $i < 0$, $i \geq m$, $j < 0$, or $j \geq n$. In the results presented, we let these equal the initial value ϕ_0 , so that the boundary can be thought to act as a stabilizing force opposing erosion. Other approaches include setting the out-of-bounds values to 0 (so that proximity to the boundary encourages erosion) or ignoring them entirely and renormalizing the kernel (so that erosion is agnostic to the boundary.) Both were investigated and showed no qualitative change in behavior aside from the degree of erosion very close to inlets and outlets.

d. Time-integration Given a solid fraction field $\phi_{i,j}$, the previous two sections detail calculation of the pressure $p_{i,j}$ and $\varphi_{i,j}$. The pressure gradient at the cell center can be calculated with a first-order finite difference stencil as

$$[\nabla p]_{i,j} = \left[\frac{(p_{i+1,j} - p_{i,j}) + (p_{i+1,j+1} - p_{i,j+1})}{2\Delta x} \right] \hat{\mathbf{x}} + \left[\frac{(p_{i,j+1} - p_{i,j}) + (p_{i+1,j+1} - p_{i+1,j})}{2\Delta y} \right] \hat{\mathbf{y}}. \quad (59)$$

Since each term on the RHS of (33a) can be calculated at cell centers given $\phi_{i,j}$, we can discretize in time so that

$$\frac{\phi_{i,j}^{n+1} - \phi_{i,j}^n}{\Delta t^n} = -\phi_{i,j}^n \max\{0, [\nabla p]_{i,j}^n - \psi(\bar{\phi}_{i,j}^n)\} =: -\phi_{i,j}^n f_{i,j}^n, \quad (60)$$

where superscripts denote time step labels and, for ease of notation, we have introduced the erosion rate f at cell center (i,j) and time step n . This corresponds to a forward Euler update

$$\phi_{i,j}^{n+1} = \phi_{i,j}^n [1 - \Delta t f_{i,j}^n], \quad (61)$$

which is not subject to any Courant–Friedrichs–Lewy (CFL) condition; the use of the convolution φ corresponds to an assumption that the loss of solid integrity due to grain dislodgement takes place on a time scale much faster than that of erosion. The choice of time step must still be handled with care; it is clear from the structure of (61) that too large a timestep will yield negative solid fractions. As such, we adopt an adaptive time-stepping algorithm utilizing Richardson extrapolation in which Δt is chosen at each time step so that the estimated error at each step falls below a specified tolerance. The method is described as follows.

Consider the time integration of an ODE $y'(t) = g(y, t)$ by a first-order forward Euler method. Letting $y_n = y(t)$, the local truncation error of a single step $y_{n+1} = y_n + g_n \Delta t$ can be written

$$\begin{aligned} y(t_n + \Delta t) &= y_n + g_n \Delta t + \frac{g'_n}{2} \Delta t^2 + \mathcal{O}(\Delta t^3), \\ &= y_{n+1} + \frac{g'_n}{2} \Delta t^2 + \mathcal{O}(\Delta t^3), \end{aligned}$$

where

$$g_n = g(y_n, t_n), \quad g'_n = \left[\frac{dg}{dt} \right]_{t=t_n}. \quad (62)$$

We can perform the same analysis for a forward Euler process of step size $\Delta t/2$. If we let

$$g_{n+\frac{1}{2}} = g\left(y_n + g_n \frac{\Delta t}{2}, t_n + \frac{\Delta t}{2}\right), \quad g'_{n+\frac{1}{2}} = \left[\frac{dg}{dt} \right]_{t=t_n + \frac{\Delta t}{2}} \quad (63)$$

Algorithm 1 Time-stepping workflow

```

initialize  $\phi_{i,j}^0$ 
set  $t \leftarrow 0$ 
set  $n \leftarrow 0$ 
set  $\Delta t \leftarrow 1$ 

while  $t < T$  do

  calculate  $p_{i,j}^n$ 
  calculate  $\varphi_{i,j}^n$ 
  set  $f_{i,j} \leftarrow \max\{0, [\nabla p]_{i,j} - \psi(\varphi_{i,j})\}$ 

  repeat

    set  $\phi_{i,j}^{n+1} \leftarrow \phi_{i,j}^n (1 - \Delta t f_{i,j})$ 
    set  $\phi_{i,j}^{n+\frac{1}{2}} \leftarrow \phi_{i,j}^n (1 - \frac{1}{2}\Delta t f_{i,j})$ 

    if  $\phi_{i,j}^{n+\frac{1}{2}} < 0$  for any  $i, j$  then
      set  $e \leftarrow \infty$ 
    else
      calculate  $p_{i,j}^{n+\frac{1}{2}}$ 
      calculate  $\varphi_{i,j}^{n+\frac{1}{2}}$ 
      set  $f_{i,j}^{n+\frac{1}{2}} \leftarrow \max\{0, [\nabla p]_{i,j}^{n+\frac{1}{2}} - \psi(\varphi_{i,j}^{n+\frac{1}{2}})\}$ 
      set  $\hat{\phi}_{i,j}^{n+1} \leftarrow \phi_{i,j}^{n+\frac{1}{2}} (1 - \frac{1}{2}\Delta t f_{i,j}^{n+\frac{1}{2}})$ 
      set  $e \leftarrow \sqrt{\frac{1}{mn} \sum_{i,j} \left( \frac{\phi_{i,j}^{n+1} - \hat{\phi}_{i,j}^{n+1}}{e_{\max}} \right)^2}$ 
    end if

    if  $e \geq 1$  then
      set  $\Delta t \leftarrow \Delta t \times \max \left\{ r_{\min}, \min \left\{ r_{\max}, \frac{r_{\text{dec}}}{\sqrt{e}} \right\} \right\}$ 
    else
      set  $\phi_{i,j}^{n+1} \leftarrow 2\hat{\phi}_{i,j}^{n+1} - \phi_{i,j}^{n+1}$ 

      if  $\phi_{i,j}^{n+1} < 0$  for any  $i, j$  then
        set  $\Delta t \leftarrow r_{\text{dec}}\Delta t$ 
        set  $e \leftarrow \infty$ 
      else
        set  $t \leftarrow t + \Delta t$ 
        set  $\Delta t \leftarrow r_{\text{inc}}\Delta t$ 
        set  $n \leftarrow n + 1$ 
      end if
    end if
  until  $e < 1$ 
end while

```

then the same truncation analysis of two steps yielding an approximated value \hat{y}_{n+1} indicates

$$\begin{aligned} y(t + \Delta t) &= y_n + \frac{\Delta t}{2} (g_n + g_{n+\frac{1}{2}}) + \frac{1}{2} \left(\frac{\Delta t}{2} \right)^2 (g'_n + g'_{n+\frac{1}{2}}) + \mathcal{O}(\Delta t^3), \\ &= \hat{y}_{n+1} + \frac{1}{2} (g'_n + g'_{n+\frac{1}{2}}) \left(\frac{\Delta t}{2} \right)^2 + \mathcal{O}(\Delta t^3), \\ &= \hat{y}_{n+1} + g'_n \left(\frac{\Delta t}{2} \right)^2 + \mathcal{O}(\Delta t^3). \end{aligned}$$

where we have assumed smooth behavior such that $g'_{n+\frac{1}{2}} = g'_n + g''_n(\Delta t/2) + \mathcal{O}(\Delta t^2)$. Combining terms, we can construct the Richardson extrapolation

$$y_{n+1}^{(R)} := 2\hat{y}_{n+1} - y_{n+1} = y(t + \Delta t) + \mathcal{O}(\Delta t^3), \quad (64)$$

which serves as one step of an integration routine with cubic truncation error: using $y_{n+1}^{(R)}$ as an update rule can be expected to yield second-order convergence in time. Moreover, subtracting one truncation analysis from the other shows that the value

$$\varepsilon_{n+1} := |\hat{y}_{n+1} - y_{n+1}| = \left| \frac{g'_n}{4} \right| \Delta t^2 + \mathcal{O}(\Delta t^3) \quad (65)$$

is the leading-order contribution to the truncation error in the $(\Delta t/2)$ -step size forward Euler update, which is assumed to represent an upper bound for that of the Richardson rule since it is $\mathcal{O}(\Delta t^2)$ as opposed to $\mathcal{O}(\Delta t^3)$; that is, we expect

$$|y(t + \Delta t) - y_{n+1}^{(R)}| \leq \varepsilon_{n+1}. \quad (66)$$

In this way, Richardson extrapolation provides second-order convergence in time as well as an estimated upper bound ε_{n+1} of the truncation error at each time step. We adapt this approach to the vector of solid fraction values $\phi_{i,j}$ by adapting (61) into two analogous forward Euler updates generated with a proposed timestep Δt_p ,

$$\phi_{i,j}^{n+1} = \phi_{i,j}^n (1 - \Delta t_p f_{i,j}^n), \quad (67)$$

$$\phi_{i,j}^{n+\frac{1}{2}} = \phi_{i,j}^n \left(1 - \frac{1}{2} \Delta t_p f_{i,j}^n \right), \quad \hat{\phi}_{i,j}^{n+1} = \phi_{i,j}^{n+\frac{1}{2}} \left(1 - \frac{1}{2} \Delta t_p f_{i,j}^{n+\frac{1}{2}} \right), \quad (68)$$

where $f_{i,j}^{n+\frac{1}{2}}$ is the erosion rate calculated as explained above given the halfway fraction $\phi_{i,j}^{n+\frac{1}{2}}$. We generalize (65) to the vector system by considering the size of the L^2 error relative to a tolerance e_{\max} , defining

$$e_k := \sqrt{\frac{1}{mn} \sum_{i,j} \left(\frac{\phi_{i,j}^k - \hat{\phi}_{i,j}^k}{e_{\max}} \right)^2}. \quad (69)$$

If $e_{n+1} \geq 1$, the proposed timestep is rejected and a smaller step is proposed; if $e_{n+1} < 1$, it is accepted and the algorithm moves to the next timestep with the Richardson update

$$\phi_{i,j}^{n+1,R} = 2\hat{\phi}_{i,j}^{n+1} - \phi_{i,j}^{n+1}. \quad (70)$$

From (65), if a timestep Δt yields an error e , we would expect a timestep $\Delta t' = \Delta t/\sqrt{e}$ to yield an error $e' \approx 1$. Accordingly, if a timestep is rejected, the timestep is reduced by a factor r_{dec}/\sqrt{e} , with $r_{\text{dec}} < 1$, subject to minimum and maximum factors $r_{\min} < r_{\text{dec}}/\sqrt{e} < r_{\max}$. If the timestep is accepted, it is increased by a factor $r_{\text{inc}} > 1$ to promote use of the largest timesteps possible. Finally, if the update produces a negative solid fraction $\phi^{n+\frac{1}{2}}$ or $\phi^{n+1,R}$, the update is aborted before the subsequent pressure calculation and the timestep is decreased by a factor r_{dec} . The process is described in Algorithm 1. The results presented in the Letter were produced with $e_{\max} = 10^{-6}$, $r_{\text{dec}} = 0.9$, $r_{\text{inc}} = 1.1$, $r_{\min} = 1/3$, and $r_{\max} = 3$.